RSC Advances

PAPER

View Article Online
View Journal | View Issue

Open Access Article. Published on 13 April 2017. Downloaded on 2/8/2026 1:18:04 AM.
This article is licensed under a Creative Commons Attribution-NonCommercial 3.0 Unported Licence.

Check for updates

Cite this: RSC Adv., 2017, 7, 21273

Photocatalytic decomposition of Rhodamine B on uranium-doped mesoporous titanium dioxide†

Yi Liu,[a] Blake Becker,[b] Brandon Burdine,[c] Ginger E. Sigmon[b] and Peter C. Burns*[ab]

Received 2nd February 2017
Accepted 7th April 2017

DOI: 10.1039/c7ra01385j

rsc.li/rsc-advances

Mesoporous uranium-doped TiO_2 anatase materials were studied to determine the influence of U-doping on the photocatalytic properties for Rhodamine B (RhB) degradation. The physico-chemical properties of the samples were characterized and the results of X-ray diffraction, transmission electron microscopy, and Raman spectroscopy demonstrate homogeneous incorporation of uranium into the anatase lattice. X-ray photoelectron spectroscopy of the doped anatase confirmed the dominance of the U^{4+} species and an increasing proportion of U^{6+} species as the uranium doping was increased. The absorption thresholds of the uranium-doped anatase extended into the visible light region. A synergistic effect of the band gap energy and oxidation state of the dopant contribute to an enhanced photocatalytic capability for RhB degradation by U-doped TiO_2.

1. Introduction

TiO_2 is a non-toxic, insoluble, and relatively inexpensive semiconductor that can be used as an active photocatalyst for reactions in aqueous solutions. Anatase is a widely studied polymorph of TiO_2, which normally exhibits high photocatalytic activity only under ultraviolet light (wavelength < 387 nm).[1,2] Extending the photo-response of anatase to the visible light region is a challenge, but would enhance the utilization efficiency of anatase-based photocatalysts using sunlight.

The response of anatase to incident light can be modified by doping metals, such as V, Cr, Fe, Ni, Zn, Cu, Co, V, Mo, Zr, Ce, and Nd.[3–8] Metal doping may introduce new energy levels between the valence band and conduction band of anatase, which narrows the band gap and inhibits the recombination of photo-excited electron–hole pairs of metal-doped anatase compared to undoped anatase.[5,9–12] Through such mechanisms, the photocatalytic properties of doped anatase under natural sun light may be improved. However, the effects of doping actinide elements, such as uranium (U), into TiO_2 and photocatalytic applications of the resulting material are understudied, although U with 5f electrons has been reported as an active catalyst for oxidation and reduction reactions. The existence of multiple readily accessible oxidation states of U and uranyl ions (UO_2^{2+}) have been reported to be photocatalytically active for oxidation of organic compounds under natural light.[13–20] Currently, only one study has investigated the influence of U doping on the photocatalytic properties of anatase.[15] Enhanced properties for quinoline photodegradation found in that study were attributed to increased optical absorption in the visible light region by U-doped anatase (TiO_2). Additional research is needed to understand how U doping affects photocatalytic properties of TiO_2.

The potential value of doping actinides into TiO_2 is understudied relative to efforts involving transition metals and lanthanides.[5,11,15,21–24] The role of 5f electrons in influencing the electronic and crystal structure of TiO_2 is largely unknown, and could preclude the application of depleted uranium in catalysts. The current study explores incorporation of uranium into TiO_2 and the use of the doped material for degradation of Rhodamine B, which is an organic dye pollutant, as a model for evaluation of the performance of U-doped TiO_2.

2. Experimental

2.1 Material preparation

2.1.1 TiO_2 preparation. Titanium isopropoxide (TTIP, 2 mL) was added to 10 mL of isopropanol during magnetic stirring for 30 minutes at room temperature. A mixture of H_2O (0.5 mL) and isopropanol (2 mL) was added to the TTIP solution (dropwise) during magnetic stirring. Once a gel formed, it was transferred to an autoclave for thermal treatment at 200 °C for 2 hours with ramping rate of 5 °C min^{-1}. The autoclave was removed from the oven and cooled to room temperature. Once cooled, the solid was recovered by filtration, washed, and dried in a 100 °C oven overnight.

2.1.2 TiU*x* preparation. TiU*x* U-doped anatase with Ti : U molar ratios of 135, 68, 45, and 34 (designated $x = 1, 2, 3$, and 4) were prepared with TTIP and uranyl nitrate hexahydrate as Ti

[a]Department of Chemistry and Biochemistry, University of Notre Dame, Notre Dame, IN 46556, USA. E-mail: pcburns@nd.edu

[b]Department of Civil & Environmental Engineering & Earth Sciences, University of Notre Dame, Notre Dame, IN 46556, USA

[c]Department of Chemical and Biomolecular Engineering, University of Notre Dame, Notre Dame, IN, 46556, USA

† Electronic supplementary information (ESI) available. See DOI: 10.1039/c7ra01385j

Open Access Article. Published on 13 April 2017. Downloaded on 2/8/2026 1:18:04 AM.
This article is licensed under a Creative Commons Attribution-NonCommercial 3.0 Unported Licence.

and U sources, respectively. Generally, TiUx samples were prepared by a method similar to the TiO_2 preparation. A solution with $UO_2(NO_3)_2 \cdot 6H_2O$, H_2O (0.5 mL) and isopropanol (2 mL) was prepared and added dropwise into a mixture of TTIP (2 mL) and isopropanol (10 mL) during magnetic stirring at room temperature. The gel-type material was transferred to an autoclave for thermal treatment from room temperature to 200 °C with a ramping rate of 5 °C min^{-1} and then held at 200 °C for 2 hours. After the autoclave cooled to room temperature, the product was obtained by filtration, washed with H_2O, and dried at 100 °C in an oven overnight.

2.2 Material characterization

Powder X-ray diffraction (XRD) measurements were conducted on a Bruker D8 Advance diffractometer equipped with CuKα radiation (40 kV and 40 mA). The diffraction patterns were collected in the 5–80° 2θ range with 0.02° steps and 1 second spent counting per step. The sample stage was rotated 15 times per minute. Lattice spacing and particle size were calculated using Bragg's equation and the Debye–Scherrer equation. Internal standards of Si and Al_2O_3 were used to calibrate peak position and peak broadening, respectively.

Raman spectra were collected on a Bruker Sentinel system with fiber optics and a video-assisted Raman probe at ambient conditions. The instrument has a 785 nm laser source and a highly sensitive charge-coupled device (CCD) detector. Spectra were obtained by scanning in the range from 80 to 3200 cm^{-1} at 400 mW for 300 s. Background was collected with a 300 s accumulation time.

The N_2 adsorption/desorption experiments were conducted on a Micromeritics ASAP 2000 at 77 K. Samples were degassed at 300 °C for 4 h in the vacuum line and then switched to the analyzing line. Specific surface area was calculated using the Brunauer–Emmett–Teller (BET) model.[25–27] Pore volumes were determined from the adsorption branch of the isotherm at a single point of $p/p_0 = 0.99$. Pore size was obtained from the adsorption branch of the isotherm by the BJH (Barrett–Joyner–Halenda) method.[25–27]

Transmission electron microscopy (TEM) was conducted using a FEI Titan 80–300 equipped with a Gatan CCD camera and an Oxford INCA LN_2 energy dispersive X-ray spectral detector with 130 eV energy resolution. Images and selected area diffraction patterns were collected at an operating voltage of 300 kV using a single tilt sample holder. Sample powders were dispersed in ethanol and sonicated for 40 minutes before being placed on the TEM grids.

Diffuse reflectance UV-Vis (DR-UV-Vis) spectra were recorded on a Jasco V-670 UV-Vis-Near IR spectrophotometer with an integrating sphere (200–2500 nm) at room temperature. The scan range was 370 to 800 nm with a 1000 nm min^{-1} scan rate, a 0.5 nm data interval, and a 5 nm bandwidth.

X-ray photoelectron spectroscopy (XPS) measurements were conducted on a PHI VersaProbe II X-ray photoelectron spectrometer at room temperature with monochromatic Al Kα radiation. The C 1s peak of adventitious carbon contamination (284.8 eV) was used for calibration.

2.3 Photodegradation of RhB experiments

For a typical photodegradation of RhB experiment, catalyst (TiO_2 or TiUx) (0.005 g) was added into a RhB aqueous solution (0.4 mg L^{-1}, 24 mL) in a 50 mL beaker. A control experiment was conducted without the addition of the catalyst. Before the photocatalytic reaction was started, the mixture was magnetically stirred in the dark for 30 min. The photodegradation reaction was carried out using a Newport solar simulator (Model 69911, output power 300 W, ozone free) with a colored glass filter that restricts the radiation to visible light (Newport, FSQ-KG3). The experiments were conducted in a dark room with ~4.0 mW power detected at the solution/catalyst location. The solar energy before and after each experiment was monitored by a Newport Optical Power Meter (Model 1916-R). Aliquots of the solutions were taken after 2 minutes under irradiation and centrifuged with glass centrifuge tubes before they were analyzed using a Jasco V-670 UV-Vis-Near IR spectrophotometer by quartz cuvettes. The scan range was 190 to 800 nm with 40 nm min^{-1} scan rate and a 5 nm bandwidth. RhB displays adsorption peaks in 440–620 nm region.

Photodegradation properties of the catalysts were evaluated by the amount of RhB decomposed, which is calculated by eqn (1). In the equation, quantity q (mg RhB per gram of catalyst) represents the amount of RhB that has been degraded, V stands for solution volume (mL), m represents the catalyst weight (g), and C_0 and C_i correspond to the concentrations of RhB in solution at the initial time and at the end of the reaction, respectively.

$$q\ (\text{mg g}^{-1}) = \frac{(C_0 - C_i) \times V}{1000m} \quad (1)$$

3. Results

3.1 XRD

The crystalline structure of the samples was verified *via* XRD. As shown in Fig. 1, both pure TiO_2 and TiUx samples have the anatase structure (JCPDS#00-064-0863). No diffraction peaks corresponding to any known uranium phases were detected for the U-doped TiO_2 samples, which suggests that U has entered

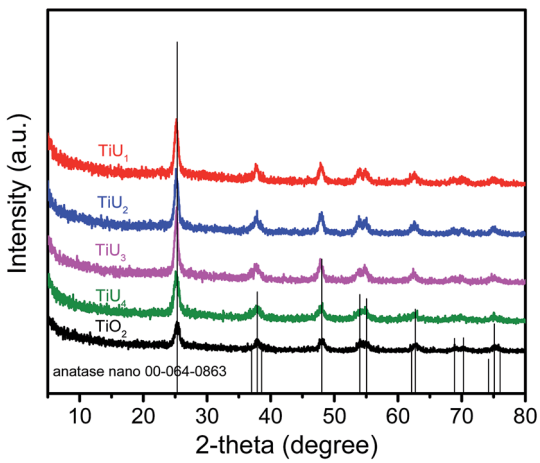

Fig. 1 XRD patterns of TiO_2 and U-doped TiO_2 (TiUx, $x = 1, 2, 3$, and 4).

Open Access Article. Published on 13 April 2017. Downloaded on 2/8/2026 1:18:04 AM.
This article is licensed under a Creative Commons Attribution-NonCommercial 3.0 Unported Licence.

the host lattice. The particle sizes of the samples are within the 9 to 13 nm region as listed in Table 1 (which are typical for mesoporous anatase).

The strong diffraction peak at 25.3° 2θ is the (101) peak of anatase. Slight shifts of the (101) reflection occur for the TiU*x* samples toward lower 2θ (Table 1), indicating expansion of the lattice due to U doping. This expansion can be attributed to the larger sizes of U^{6+} and U^{4+} (87 pm and 103 pm in 6-coordinate, respectively) compared to that of Ti^{4+} (74.5 pm) in the anatase phase.[28] Increases in the lattice spacing of TiO_2 have been reported in metal doped TiO_2 due to the larger ionic radii of the metal dopants (Ce,Zr).[5]

3.2 Raman spectroscopy

To further explore if U had been incorporated into the TiO_2 lattice, the samples were characterized by Raman spectroscopy. Raman spectra of all samples demonstrate characteristic vibration signals for the anatase phase at 145 cm^{-1} (E_g), 196 cm^{-1} (E_g), 397 cm^{-1} (B_{1g}), 516 cm^{-1} ($B_{1g} + A_{1g}$) and 638 cm^{-1} (E_g) (Fig. 2a).[29] No Raman signals for the T_{2g} mode of UO_2 (445 cm^{-1}) and symmetric stretching vibration mode of the uranyl group UO_2^{2+} (840 cm^{-1}) typical of uranium phases were detected.[30,31] This indicates U was likely incorporated into the TiO_2 matrix.

The Raman peak centered at 145 cm^{-1} is shown in Fig. 2b. The peak centers of TiU1 to TiU4 are blue-shifted relative to that of TiO_2, and the shifts become larger sequentially as the U-doping amounts increase. The peaks of TiU1 to TiU4 are broader than that of TiO_2. The blue-shift and broader bandwidth of the peak at 145 cm^{-1} can be ascribed to structural disorder generated by U-doping.[32] Therefore, the absence of UO_2^{2+} vibrations, along with the presence of peak shifting and peak broadening, further verify that U has been incorporated in the TiO_2 lattice.

3.3 TEM

TEM was used to gain information on sample morphology, particle size, crystal structure, and elemental composition. TiU4 (corresponding to the highest U-doping) has a nanoparticle morphology (Fig. 3). All other samples had similar morphologies and are shown in Fig. S1.† The average particle size for all samples range from 11 nm to 14 nm and compare well with the particle sizes calculated based on XRD data.

The crystal structures of the samples were characterized by selected-area electron diffraction (SAED) in the TEM. The SAED pattern of TiU4 is shown as the inserted image in Fig. 3b, and is attributed to the anatase TiO_2 phase from the circled area. No other TiO_2 phase or uranium phases were detected. The elemental composition of the circled area in Fig. 3b was examined by energy-dispersive spectroscopy (EDS). The EDS spectrum in Fig. S2a† exhibits a characteristic U signal and Ti signals. The results of SAED and EDS corroborate that U atoms have been homogeneously distributed in the TiO_2 sample without noticeable phase separations of TiO_2 and U-composites. This is further supported by analyses of scanning-transmission electron microscopy (STEM) and EDS spectra of two selected points of TiU4 (shown in Fig. S2b–d†), which do not reveal any U-compounds. The SAED, EDS, and STEM

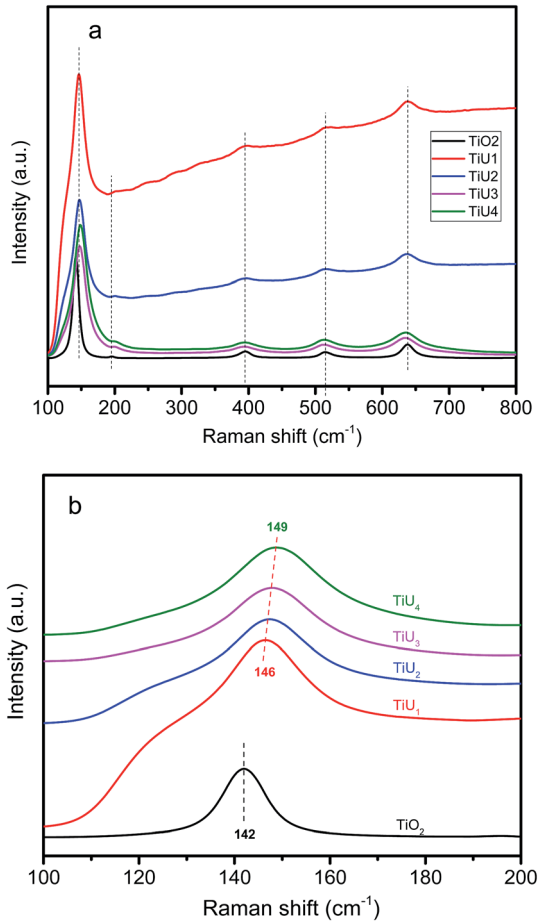

Fig. 2 Raman spectra of samples in (a) 100–800 cm^{-1} range and (b) 100–200 cm^{-1} range.

Table 1 Particle size derived from XRD data for TiO_2 and TiU*x* (*x* = 1, 2, 3, and 4) and average particle size of samples obtained by TEM analyses

Samples	2θ (°)	FWHM (radian)	Particle size (nm)	*d*-Spacing (Å)	Average particle size from TEM (nm)
TiO_2	25.30	0.012	12	3.518	12 ± 2
TiU1	25.25	0.011	13	3.524	11 ± 2
TiU2	25.26	0.011	12	3.523	14 ± 2
TiU3	25.24	0.011	13	3.526	13 ± 2
TiU4	25.27	0.015	9	3.521	11 ± 1

Open Access Article. Published on 13 April 2017. Downloaded on 2/8/2026 1:18:04 AM.
This article is licensed under a Creative Commons Attribution-NonCommercial 3.0 Unported Licence.

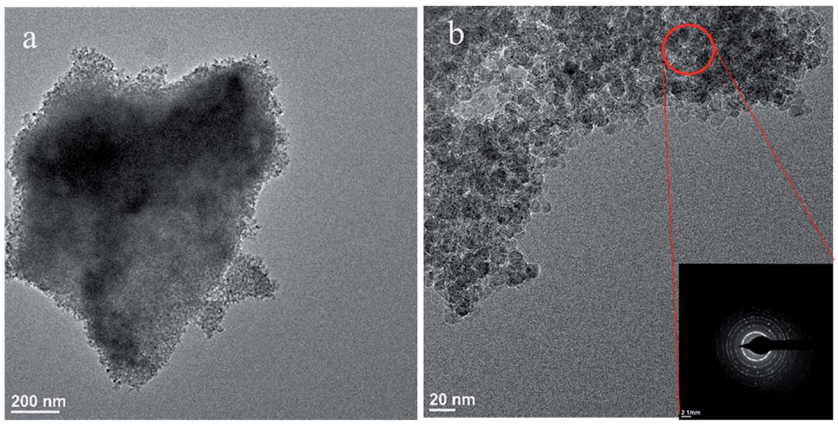

Fig. 3 TEM images of TiU4 (a) and (b) with inserted SAED pattern of the circled area.

analyses were also done on other samples. Similar results were obtained and all samples exhibit only the anatase phase. U atoms were homogeneously distributed in anatase TiO_2 without detectable separated phases of U-composites.

3.4 N_2 adsorption/desorption

Surface area is an important factor governing the catalytic activity of a material, as the surface is where the reactions take place. Higher surface area generally corresponds to higher catalytic activity. Sample surface area and pore properties were analyzed by N_2 adsorption and desorption experiments. Sorption isotherms (Fig. 4) are typical of type IV curves with H2 type hysteresis loops.[33] This type of isotherm is the characteristic feature of mesoporous structures. Detailed results from N_2 adsorption/desorption including surface area, pore volume, and pore size distribution are listed in Table 2. The surface area of TiO_2 as prepared is 71 $m^2\ g^{-1}$, and this is much larger than that of commercial anatase (1 $m^2\ g^{-1}$, purchased from JT Baker without further treatment). All U-doped samples have surface area larger than 90 $m^2\ g^{-1}$ and surface area increases as the U concentration rises. The pore size distributions are all within the mesoscale range (2–50 nm), and the pore size decreases as the U doping increases. The exact mechanism of pore tuning by U doping in the TiU*x* samples remains unclear. Possible pore formation mechanisms can be attributed to the hydrolysis of the TTIP, which could be influenced by the quantity of uranyl nitrate, the U precursor. Uranyl nitrate is acidic, and thus the acidity of the solution increases as it is added. The acidity impacts the hydrolysis rate of the TTIP, which is one crucial step in the formation of mesoporous titania-based oxides.[3,34,35] Pore sizes of TiO_2 prepared under acidic conditions are smaller than that made in neutral and basic conditions.[34]

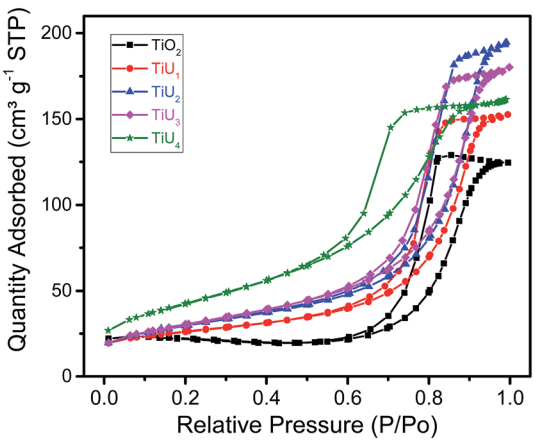

Fig. 4 Sorption isotherms of samples collected by N_2 adsorption/desorption experiments.

3.5 XPS

XPS data of each prepared sample were collected to investigate the surface chemistry. Each data collection was referenced to the C 1s peak at 284.8 eV. The XPS spectra of Ti 2p, U 4f, and O 1s of TiU*x* are shown in Fig. 5. The Ti 2p spectra in Fig. 5a shows core level binding energies at around 463.9 eV and 458.2 eV, which can be indexed to Ti $2p_{1/2}$ and Ti $2p_{3/2}$ of the Ti^{4+} state in TiO_2.[5,36–39] In Fig. 5b, the strong O 1s peaks at 529.8 eV are attributed to the Ti–O bonds in the TiO_2 lattice, and the shoulder peaks at around 531.6 eV are related to surface hydroxyl groups.[5,36–38] All samples exhibit identical Ti 2p and O 1s spectra, which indicates the oxidation states (Ti^{4+}) and oxygen species (lattice oxygen and surface hydroxyl groups of TiO_2) are the same for TiU1 through TiU4.

The difference in surface chemistry, however, resides in the oxidation state of U. The U 4f spectra are shown in Fig. 5c. TiU1

Table 2 Surface areas, pore volumes, and pore sizes of TiO_2 and TiU*x* (*x* = 1, 2, 3, and 4)

Samples	Surface area ($m^2\ g^{-1}$)	Pore volume ($cm^3\ g^{-1}$)	Pore size (nm)
TiO_2	71	0.19	13
TiU1	92	0.24	12
TiU2	106	0.30	11
TiU3	109	0.28	9
TiU4	154	0.25	6

 This journal is © The Royal Society of Chemistry 2017

Open Access Article. Published on 13 April 2017. Downloaded on 2/8/2026 1:18:04 AM.
This article is licensed under a Creative Commons Attribution-NonCommercial 3.0 Unported Licence.

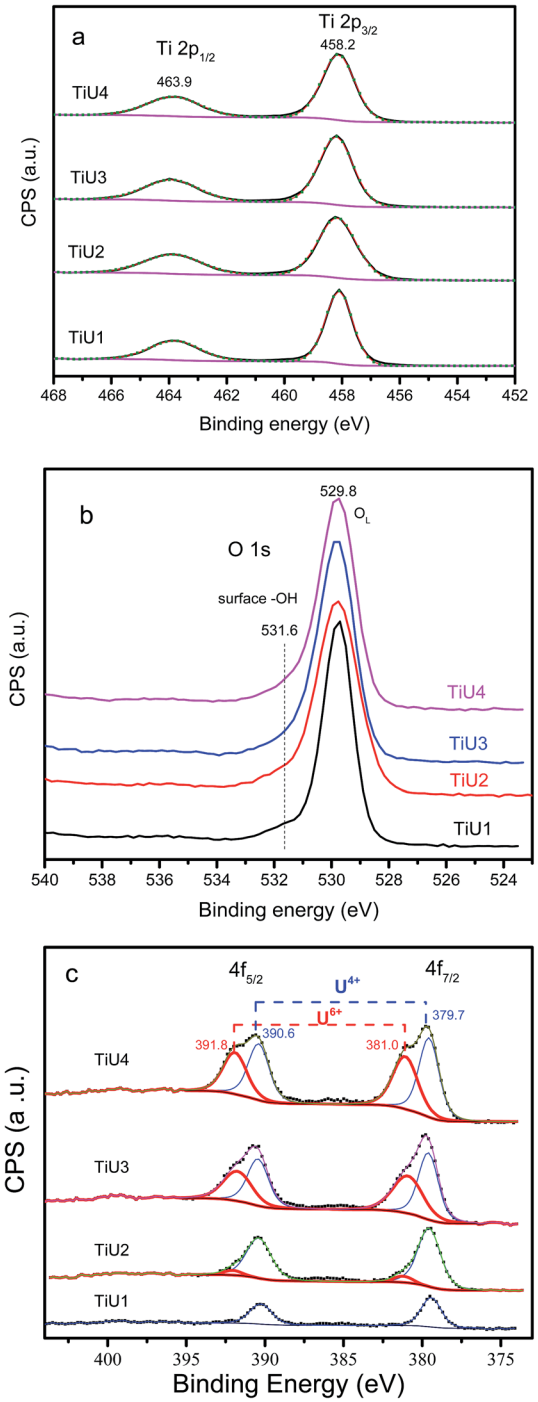

Fig. 5 XPS spectra of (a) Ti 2p, (b) O 1s, and (c) U 4f of TiUx (x = 1, 2, 3, and 4).

has peaks at binding energies 390.6 eV and 379.7 eV, which correspond to the U $4f_{5/2}$ and U $4f_{7/2}$ signals of U^{4+}, respectively.[40–42] The U spectra of TiU2, TiU3, and TiU4 show peaks at 391.8 eV and 381.0 eV, corresponding to the U $4f_{5/2}$ and U $4f_{7/2}$ signals of U^{6+}, respectively, in addition to the U^{4+} signal.[40–42] This indicates that higher U doping caused the samples to contain mixed U oxidation states (4+ and 6+). The atomic ratio of $U^{4+}/(U^{4+} + U^{6+})$ in TiU1, TiU2, TiU3, and TiU4 decreases from 100%, 90%, 72%, to 62% as listed in Table 3. The U^{4+} species are stable and detectable in ambient conditions based on the results of UV-Vis reflectance spectra shown in Fig. S3.†[43,44] The change of U oxidation states from U^{6+} in the U precursor to U^{4+} in the TiUx samples likely results from reduction of the uranyl nitrate by organic solvents during the synthesis.[18,45] Different oxidation states of the dopants in metal precursors and prepared doped-TiO_2 were also observed in U-, Ce-, and Fe-doped TiO_2.[10,15,39]

3.6 DR-UV-Vis

The optical absorption spectra of pristine TiO_2 and U-doped TiO_2 are shown in Fig. 6. The absorption thresholds were determined as the tangent line intercepts with the wavelength axis as shown in Fig. 6a. All U-doped TiO_2 samples exhibited spectra with absorption thresholds (429 nm to 495 nm) extended into the visible light region, as compared to TiO_2 (403 nm), which reveals a remarkable enhancement in the visible light absorption of the TiUx samples.[5,21] The indirect band gap energies were obtained by converting DR-UV-Vis data into a Kubelka–Munk function plotted against the photon energy ($h\nu$).[46,47] The intersections of tangent lines of each curve with the horizontal axis give the band gap energy of each sample as shown in Fig. 6b, and the band gap energies are listed in Table 3. The band gap energy of undoped TiO_2 was found to be 3.0 eV, which is in good agreement with the reported value for anatase TiO_2 (3.1–3.2 eV).[39,48–50] Incorporation of U into the TiO_2 matrix leads to a narrower band gap, and the TiU3 sample has the lowest band gap energy (2.0 eV). These results show that a small amount of U-doping can significantly modify the band gap structure of TiO_2.

3.7 Photodegradation of RhB

The RhB removal for the TiUx samples under visible light is shown in Fig. 7. TiU1 has a similar activity as TiO_2, while TiU2, TiU3, and TiU4 exhibit a higher capacity for RhB degradation than TiO_2, and the photocatalysis performance increased as the sequence TiU4 < TiU3 < TiU2. TiU2 is the optimal photocatalyst for RhB removal under the experimental conditions, which indicates that the photocatalytic properties of U-doped TiO_2 do not monotonously increase as the U-doping amount is increased. This is consistent with studies on metal doped-TiO_2 as photocatalysts, in which excess dopants will trap the photogenerated charge carriers for recombination.[4,15,51]

Table 3 Optical absorption edge, band gap energy, and $U^{4+}/(U^{4+} + U^{6+})$ atomic ratio of TiO_2 and TiUx (x = 1, 2, 3, and 4)

Samples	Absorption edge (nm)	Band gap (eV)	$U^{4+}/(U^{4+} + U^{6+})$ at. ratio (%)
TiO_2	403	3.0	—
TiU1	429	2.5	100
TiU2	460	2.3	90
TiU3	495	2.0	72
TiU4	456	2.2	62

Open Access Article. Published on 13 April 2017. Downloaded on 2/8/2026 1:18:04 AM.
This article is licensed under a Creative Commons Attribution-NonCommercial 3.0 Unported Licence.

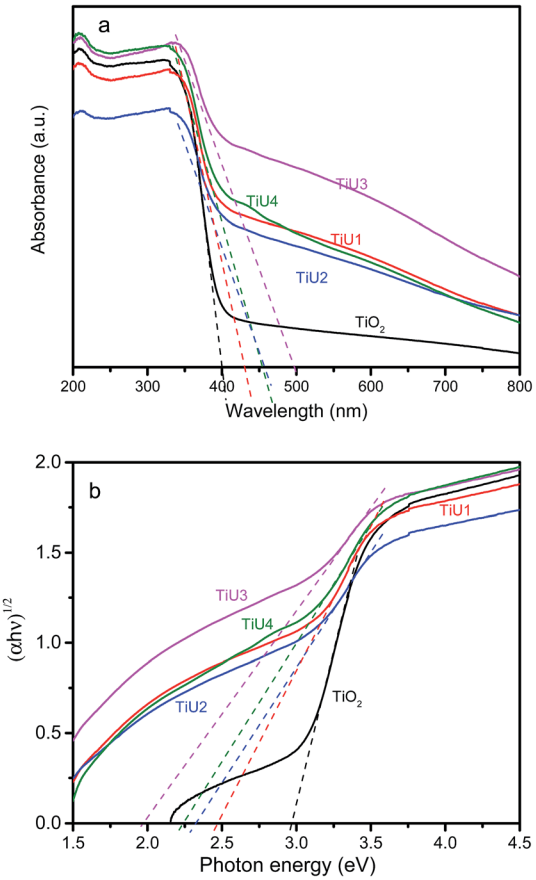

Fig. 6 DR-UV-Vis spectra of TiO_2 and TiU*x* ($x = 1$, 2, 3, and 4).

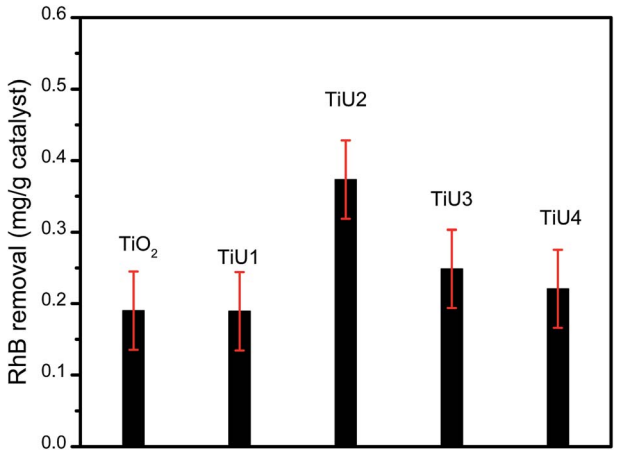

Fig. 7 RhB removal by catalyst (mg g^{-1}) under visible light. The error bars represent standard deviation.

4. Discussion

RhB photodegradation performance of TiO_2 was improved by U-doping. The mechanism of how metal dopant influences the photocatalytic performance of TiO_2 is likely complicated. In addition to the surface area and crystal structure, factors such as band gap energy, oxidation state of the dopant, and recombination of the photo-generated electron–hole pairs may be responsible for the improved photocatalytic properties of doped TiO_2.[1,5,39,51–54]

Both pure TiO_2 and U-doped TiO_2 samples are the anatase phase, as shown by the XRD and Raman spectroscopy. A direct correlation between the surface areas/pore sizes and the U doping level in the mesoporous TiO_2 and TiU*x* samples was observed. Larger surface area and a small particle size of TiO_2 allows more ready access of photo-excited electron–hole pairs on the catalyst surface.[1,55] However, evaluating the relationship between the surface area/pore sizes and RhB photodegradation performance of the samples suggests neither the surface area nor the pore size of mesoporous samples exhibits a direct influence on RhB photodegradation properties.

The data from the RhB photodegradation and the DR-UV-Vis spectra suggest the band gap drastically affects the photocatalytic capability of U-doped TiO_2. TiU1, TiU2, and TiU3 have lower band gap energies (2.5 eV, 2.3 eV, and 2.0 eV, respectively) than TiO_2, which corresponds to better RhB removal. Furthermore, TiU2, TiU3, and TiU4 exhibited higher capability for RhB removal than TiU1. The narrower band gap of the photocatalyst allows better utilization of visible light during the RhB photodegradation reaction after U-doping, and this is consistent with literature reports.[10,39] For example, Fe^{3+}-doped TiO_2 exhibited a red-shifted absorption edge toward the visible region, which was responsible for improved performance of photodegradation of methylene blue and 4-chlorophenol under visible light.[39] This is also reported in the case of Ce-doped TiO_2, which showed an improved photocatalytic capability for nitrobenzene degradation under visible light because of a narrowed band gap after Ce-doping.[10]

The improved optical absorption ability of U-doped TiO_2 for visible light does not guarantee the doped catalyst has better photocatalytic properties. TiU3 showed a weaker capability for RhB removal than TiU2, even though it had a lower band gap energy. This can be attributed to the influence of the oxidation state of U present in the sample. The increased amount of U^{6+} diminished the photocatalytic performance for RhB degradation under visible light. In TiU3 and TiU4, 72% and 62% of the U was U^{4+}, respectively, whereas for TiU2 90% of the U was U^{4+}, which correlates to a reduced capability for RhB photodegradtion on TiU3 and TiU4 in comparison to that on TiU2. The influence of U oxidation state on photocatalytic properties can be attributed to modifying the band gap structure of anatase TiO_2, which has been reported in other transition metal doped-TiO_2.[11,54]

Theoretical studies indicate that a lower oxidation state of a transition metal can enhance photocatalytic performance by introducing oxygen vacancies. For example, in the case of Mo-doped TiO_2, Mo^{5+} (instead of Mo^{6+}) is associated with the presence of oxygen vacancies that were possible electron donors.[54] These oxygen vacancies created by doping metal ions into TiO_2 play an essential role in non-dissociative adsorption of O_2 to form oxidative superoxide (O_2^-), which facilitates the photocatalytic oxidation.[56] U^{4+} (instead of U^{6+}) is expected to possess a similar capacity to decrease the band gap, which is consistent with our UV-Vis results.

Open Access Article. Published on 13 April 2017. Downloaded on 2/8/2026 1:18:04 AM.
This article is licensed under a Creative Commons Attribution-NonCommercial 3.0 Unported Licence.

A higher oxidation state of a transition metal is often detrimental to photocatalytic activity.[11] From another perspective, the U^{6+} may act as a trap for photo-generated electrons, which further recombine with photo-generated holes to reduce the efficiency for solar light utilization. An example from Choi *et al.* demonstrates that V^{5+} trapped electrons that resulted in a significantly lower photocatalytic activity of V^{5+}, compared to that of V^{4+} in V-doped TiO_2.[11] Therefore, a synergistic effect of the band gap energy and oxidation state principally contributes to the photocatalytic capability for the RhB degradation in the U-doped TiO_2.

Dye-sensitization of TiU*x* catalysts also possibly are important in improved RhB removal under visible light irradiation.[1,57] RhB is adsorbed to catalyst surfaces through linking of carboxyl groups in RhB to the surface hydroxyl groups of titania based catalysts.[3] Under visible light irradiation, excited electrons of RhB are transferred to the catalyst surface and the surface uranium species act as electron traps to avoid recombination of photo-generated electron–hole pairs.[1,3] This dye-sensitization on the catalyst may provide enhanced activity of the catalyst for RhB removal under visible light.

5. Conclusions

The 5f element uranium has been used as a dopant in TiO_2 in an attempt to enhance photocatalytic reactions. Results show that uranium dopants in anatase modify the band gap structure and influence the photocatalytic degradation of RhB under visible light irradiation. Results of extensive characterization are consistent with the homogeneous distribution of uranium in the doped materials for the low doping ratio of uranium used here (<2.9 atomic%). All U-doped samples exhibit extended optical absorption thresholds to visible light. The band gap energy and the oxidation state of U synergistically impact the photocatalytic properties of the U-doped TiO_2 for RhB degradation. Narrower band gaps and lower U^{6+} in the U-doped TiO_2 result in better photocatalytic properties. Dye-sensitization may enhanced photocatalytic activities of U-doped TiO_2 under visible light.

Acknowledgements

This work was supported by the Department of Energy, Basic Energy Sciences, Energy Frontier Research Center under the award number DE-SC0001089. Diffraction, Raman, XPS, DR-UV-Vis data were collected at the Materials Characterization Facility, Center for Sustainable Energy at Notre Dame. TEM data collected at the Notre Dame Integrated Imaging Facility. BET data collected at the Center for Environmental Science and Technology at Notre Dame.

Notes and references

1 V. Etacheri, C. D. Valentin, J. Schneider, D. Bahnemann and S. C. Pillai, *J. Photochem. Photobiol., C*, 2015, **25**, 1–29.
2 D. A. H. Hanaor and C. C. Sorrell, *J. Mater. Sci.*, 2011, **46**, 855–874.
3 X. B. Chen and S. S. Mao, *Chem. Rev.*, 2007, **107**, 2891–2959.
4 M. A. Rauf, M. A. Meetani and S. Hisaindee, *Desalination*, 2011, **276**, 13–27.
5 K. Nagaveni, M. S. Hegde and G. Madras, *J. Phys. Chem. B*, 2004, **108**, 20204–20212.
6 Y. C. Nah, I. Paramasivam and P. Schmuki, *ChemPhysChem*, 2010, **11**, 2698–2713.
7 B. F. Gao, T. M. Lim, D. P. Subagio and T. T. Lim, *Appl. Catal., A*, 2010, **375**, 107–115.
8 T. D. Pham and B. K. Lee, *Appl. Catal., A*, 2017, **529**, 40–48.
9 J. R. Chen, F. X. Qiu, W. Z. Xu, S. S. Cao and H. J. Zhu, *Appl. Catal., A*, 2015, **495**, 131–140.
10 P. Ellappan and L. R. Miranda, *Int. J. Photoenergy*, 2014, **2014**, 1–9.
11 W. Y. Choi, A. Termin and M. R. Hoffmann, *J. Phys. Chem.*, 1994, **98**, 13669–13679.
12 B. Liu, H. M. Chen, C. Liu, S. C. Andrews, C. Hahn and P. D. Yang, *J. Am. Chem. Soc.*, 2013, **135**, 9995–9998.
13 Z. R. Ismagilov, S. V. Kuntsevich, N. V. Shikina, V. V. Kuznetsov, M. A. Kerzhentsev, V. A. Ushakov, V. A. Rogov, A. I. Boronin and V. I. Zaikovsky, *Catal. Today*, 2010, **157**, 217–222.
14 Z. R. Ismagilov and S. V. Lazareva, *Catal. Rev.*, 2013, **55**, 135–209.
15 S. Y. Liu and Q. G. Feng, *Adv. Mater. Res.*, 2011, **148–149**, 1208–1211.
16 K. Vidya, V. S. Kamble, P. Selvam and N. M. Gupta, *Appl. Catal., B*, 2004, **54**, 145–154.
17 K. Vidya, V. S. Kamble, N. M. Gupta and P. Selvam, *J. Catal.*, 2007, **247**, 1–19.
18 S. L. Suib, A. Kostapapas and D. Psaras, *J. Am. Chem. Soc.*, 1984, **106**, 1614–1620.
19 J. A. Nieweg, K. Lemma, B. G. Trewyn, V. S. Y. Lin and A. Bakac, *Inorg. Chem.*, 2005, **44**, 5641–5648.
20 P. L. Arnold and Z. R. Turner, *Nature Reviews Chemistry*, 2017, **1**, 0002.
21 G. Liu, L. Z. Wang, H. G. Yang, H. M. Cheng and G. Q. Lu, *J. Mater. Chem.*, 2010, **20**, 831–843.
22 Y. Q. Wang, R. R. Zhang, J. B. Li, L. L. Li and S. W. Lin, *Nanoscale Res. Lett.*, 2014, **9**, 46.
23 M. Saif and M. S. A. Abdel-Mottaleb, *Inorg. Chim. Acta*, 2007, **360**, 2863–2874.
24 A. W. Xu, Y. Gao and H. Q. Liu, *J. Catal.*, 2002, **207**, 151–157.
25 M. Kruk, M. Jaroniec, C. H. Ko and R. Ryoo, *Chem. Mater.*, 2000, **12**, 1961–1968.
26 K. Zhang, L. L. Xu, J. G. Jiang, N. Calin, K. F. Lam, S. J. Zhang, H. H. Wu, G. D. Wu, B. Albela, L. Bonneviot and P. Wu, *J. Am. Chem. Soc.*, 2013, **135**, 2427–2430.
27 J. W. Lee, M. C. Orilall, S. C. Warren, M. Kamperman, F. J. DiSalvo and U. Wiesner, *Nat. Mater.*, 2008, **7**, 222–228.
28 R. Shannon, *Acta Crystallogr., Sect. A: Cryst. Phys., Diffr., Theor. Gen. Crystallogr.*, 1976, **32**, 751–767.
29 J. Zhang, M. J. Li, Z. C. Feng, J. Chen and C. Li, *J. Phys. Chem. B*, 2006, **110**, 927–935.
30 G. C. Allen, I. S. Butler and T. Nguyen Anh, *J. Nucl. Mater.*, 1987, **144**, 17–19.

Open Access Article. Published on 13 April 2017. Downloaded on 2/8/2026 1:18:04 AM.
This article is licensed under a Creative Commons Attribution-NonCommercial 3.0 Unported Licence.

31 L. E. Sweet, T. A. Blake, C. H. Henager Jr, S. Y. Hu, T. J. Johnson, D. E. Meier, S. M. Peper and J. M. Schwantes, *J. Radioanal. Nucl. Chem.*, 2013, **296**, 105–110.
32 N. D. Feng, F. Liu, M. Huang, A. M. Zheng, Q. Wang, T. H. Chen, G. Y. Cao, J. Xu, J. Fan and F. Deng, *Sci. Rep.*, 2016, **6**, 34765.
33 K. S. W. Sing, D. H. Everett, R. A. W. Haul, L. Moscou, R. A. Pierotti, J. Rouquerol and T. Siemieniewska, *Pure Appl. Chem.*, 1985, **57**, 603–619.
34 J. G. Yu, J. C. Yu, M. K. P. Leung, W. K. Ho, B. Cheng, X. J. Zhao and J. Z. Zhao, *J. Catal.*, 2003, **217**, 69–78.
35 X. Zhang, H. Yang, F. Zhang and K. Y. Chan, *Mater. Lett.*, 2007, **61**, 2231–2234.
36 M. V. Dozzi, S. Marzorati, M. Longhi, M. Coduri, L. Artiglia and E. Selli, *Appl. Catal., B*, 2016, **186**, 157–165.
37 C. C. Chen, H. L. Bai and C. L. Chang, *J. Phys. Chem. C*, 2007, **111**, 15228–15235.
38 P. H. Wang, P. S. Yap and T. T. Lim, *Appl. Catal., A*, 2011, **399**, 252–261.
39 H. Khan and I. K. Swati, *Ind. Eng. Chem. Res.*, 2016, **55**, 6619–6633.
40 K. Yuan, E. S. Ilton, M. R. Antonio, Z. R. Li, P. J. Cook and U. Becker, *Environ. Sci. Technol.*, 2015, **49**, 6206–6213.
41 F. X. Zhang, M. Lang, J. W. Wang, W. X. Li, K. Sun, V. Prakapenka and R. C. Ewing, *J. Solid State Chem.*, 2014, **213**, 110–115.
42 J. H. Yeon, M. D. Smith, J. Tapp, A. Möller and H. C. zur Loye, *J. Solid State Chem.*, 2016, **236**, 83–88.
43 E. Hashem, A. N. Swinburne, C. Schulzke, R. C. Evans, J. A. Platts, A. Kerridge, L. S. Natrajan and R. J. Baker, *RSC Adv.*, 2013, **3**, 4350–4361.
44 S. I. Nikitenko, C. Cannes, C. Le Naour, P. Moisy and D. Trubert, *Inorg. Chem.*, 2005, **44**, 9497–9505.
45 S. Tsushima, *Inorg. Chem.*, 2009, **48**, 4856–4862.
46 Y. Zhang, Z. P. Xing, X. F. Liu, Z. Z. Li, X. Y. Wu, J. J. Jiang, M. Li, Q. Zhu and W. Zhou, *ACS Appl. Mater. Interfaces*, 2016, **8**, 26851–26859.
47 J. Q. Bai, W. Wen and J. M. Wu, *CrystEngComm*, 2016, **18**, 1847–1853.
48 D. S. Gopala, R. R. Bhattacharjee, R. Haerr, B. Yeginoglu, O. D. Pavel, B. Cojocaru, V. I. Parvulescu and R. M. Richards, *ChemCatChem*, 2011, **3**, 408–416.
49 L. C. Chen, C. M. Huang, C. S. Gao, G. W. Wang and M. C. Hsiao, *Chem. Eng. J.*, 2011, **175**, 49–55.
50 G. Fu, P. Zhou, M. M. Zhao, W. D. Zhu, S. C. Yan, T. Yu and Z. G. Zou, *Dalton Trans.*, 2015, **44**, 12812–12817.
51 I. Medina-Ramírez, J. L. Liu, A. Hernández-Ramírez, C. Romo-Bernal, G. Pedroza-Herrera, J. Jáuregui-Rincón and M. A. Gracia-Pinilla, *J. Mater. Sci.*, 2014, **49**, 5309–5323.
52 T. Berger, M. Sterrer, O. Diwald, E. Knözinger, D. Panayotov, T. L. Thompson and J. T. Yates, *J. Phys. Chem. B*, 2005, **109**, 6061–6068.
53 W. Y. Choi, A. Termin and M. R. Hoffmann, *J. Phys. Chem.*, 1994, **98**, 13669–13679.
54 M. Matsubara, R. Saniz, B. Partoens and D. Lamoen, *Phys. Chem. Chem. Phys.*, 2017, **19**, 1945–1952.
55 S. Larumbe, M. Monge and C. Gómez-Polo, *Appl. Surf. Sci.*, 2015, **327**, 490–497.
56 T. Thompson and J. T. Yates, *Top. Catal.*, 2005, **35**, 197–210.
57 M. Quintana, T. Edvinsson, A. Hagfeldt and G. Boschloo, *J. Phys. Chem. C*, 2006, **111**, 1035–1041.

 This journal is © The Royal Society of Chemistry 2017